Modeling the effect of notch geometry on the deformation of a strongly anisotropic aluminum alloy

Oana Cazacu[1,*], Nitin Chandola[1], Benoit Revil-Baudard[1], Bjørn Håkon Frodal[2], Tore Børvik[2,3] and Odd Sture Hopperstad[2,3]

[1] *Department of Mechanical and Aerospace Engineering, University of Florida, REEF, 1350N. Poquito Rd., Shalimar, FL 32579, USA*

[2] *Structural Impact Laboratory (SIMLab), Department of Structural Engineering, Norwegian University of Science and Technology (NTNU), NO-7491 Trondheim, Norway*

[3] *Centre for Advanced Structural Analysis (CASA), NTNU, NO-7491 Trondheim, Norway*

Abstract

In this study, an elastic-plastic model with yielding described by a newly proposed orthotropic yield criterion was used to model the unusual deformation of a strongly textured AA6060 alloy. Available experimental data from tension tests and results of crystal plasticity simulations were used to determine the anisotropy coefficients involved in the yield criterion. Virtual material tests using a recent polycrystalline model were performed to obtain flow stresses for loadings where experimental data were not available. The capability of the elastic-plastic model to account for the distinct anisotropy of the material is demonstrated through comparison of finite element simulations and experimental tests on both smooth and notched axisymmetric specimens of the AA6060 alloy. Specifically, for the smooth specimen, the model predicts that the minimum cross-section evolves from a circle to an ellipse while for the notched specimens, the minimum cross-section evolves from a circular shape to an approximately rectangular, or rhomboidal shape, respectively as observed in the experiments. This model can be easily implemented in finite element codes, requires reduced CPU time compared to crystal plasticity finite element simulations, and can be applied in simulations of large-scale structural applications.

Keywords: Orthotropic plasticity; Polycrystalline model; Notch effects; Single-crystal criterion

---

[*] Corresponding author.

e-mail address: cazacu@reef.ufl.edu (O. Cazacu)

1. Introduction

Aluminum alloys of the 6000-series are used in building structures and automotive parts where light weight is a design criterion. To reduce the weight of a structure or a structural component, it is necessary to fully utilize the strength and ductility of the alloy. The credibility of the finite element (FE) analysis depends critically on the constitutive models used to describe plastic deformation and fracture of the structural material. In addition to being sufficiently accurate, the constitutive models must be robust and efficient to achieve acceptable computation times.

A challenge with many rolled and extruded aluminum alloys is the strong anisotropy, where the flow stress, plastic strain and ductility depend markedly on the loading direction with respect to the principal axes of anisotropy (Fourmeau et al. (2011, 2013)). The plastic anisotropy, i.e., the directional dependence of the flow stress and plastic strain, is largely determined by the crystallographic texture of the alloy (Engler and Randle, 2009) and is well described by polycrystal plasticity (K. Zhang et al. (2015); H. Zhang et al. (2016); Kohar et al. (2019)). Also the ductility depends on the crystallographic texture (Morin et al. (2018)), but other features like the volume fraction and size distribution of constituent particles, the yield stress and the grain size are equally important (Hannard et al. (2016); Frodal et al. (2017)). Extruded aluminum alloys have typically either recrystallized, equi-axed or non-recrystallized, fibrous grain structure. The accompanying crystallographic texture is a strong cube texture with a minor Goss component, or a deformation texture with a cube component in addition to components along the β-fiber (Frodal et al. (2017)).

Khadyko et al. (2015) performed FE simulations of smooth and notched tension tests for an extruded AA6060 aluminum alloy exhibiting a strong cube texture with a minor Goss component, and compared the numerical results with experiments. A particularly interesting observation from the experiments on this extruded material was that the notched specimens developed a rhomboid shape, which is unusual and attributed to the strong crystallographic texture of the alloy. The FE simulations were carried out using either a macroscopic elastic-plastic model with the Yld2004-18p orthotropic yield surface (Barlat et al. (2005)) or a crystal plasticity model. The anisotropic yield surface of the macroscopic model was determined based on full-constraint Taylor simulations using the crystal plasticity model combined with the initial texture of the alloy. For both models, the work hardening response was determined from tensile

2

tests on smooth specimens. The crystal plasticity finite element (CP-FE) simulations captured the complex cross-sectional geometry of the specimens after large deformations, whereas this was not the case for the simulations with the Yld2004-18p yield criterion. However, CP-FE calculations are computationally very intensive, thus limiting the applicability of this approach to large-scale structural applications.

In this paper, the deformation up to failure of this strongly textured AA6060 alloy is modeled using an elastic-plastic model with yielding described by the orthotropic yield criterion of Cazacu (2018) and isotropic hardening. To determine the anisotropy coefficients involved in this criterion we use available experimental data from tension tests and results of crystal plasticity simulations. Specifically, to obtain flow stresses for loadings where experimental data were not available we use the recent polycrystalline model of Chandola et al. (2017) which is based on the single crystal criterion of Cazacu et al. (2018). The capability of the macroscopic elastic-plastic model to account for the pronounced anisotropy of the material is demonstrated through comparison between the FE simulations and the experimental data obtained in tension tests on axisymmetric specimens of both smooth and notched geometries by Khadyko et al. (2015). It is for example shown that the Cazacu (2018) model describes correctly the influence of the notched geometry on the deformation. In particular, the unusual post-test geometry of the specimens is predicted with good accuracy. Moreover, the elastic-plastic model can be easily implemented in FE codes, requires reduced CPU time compared to CP-FE models, and can be applied routinely for detailed analyses of complex processes.

2. Material

The material used to identify the parameters of the polycrystal plasticity model and the macroscopic elastic-plastic model, is an AA6060 alloy. The material was delivered as extruded profiles with 10 mm thickness and 83 mm width and had a recrystallized structure with grains slightly elongated in the extrusion direction. The average grain size was 60–70 μm. The extruded AA6060 alloy exhibited a strong recrystallization texture, as evidenced by the pole figures shown in Figure 1.
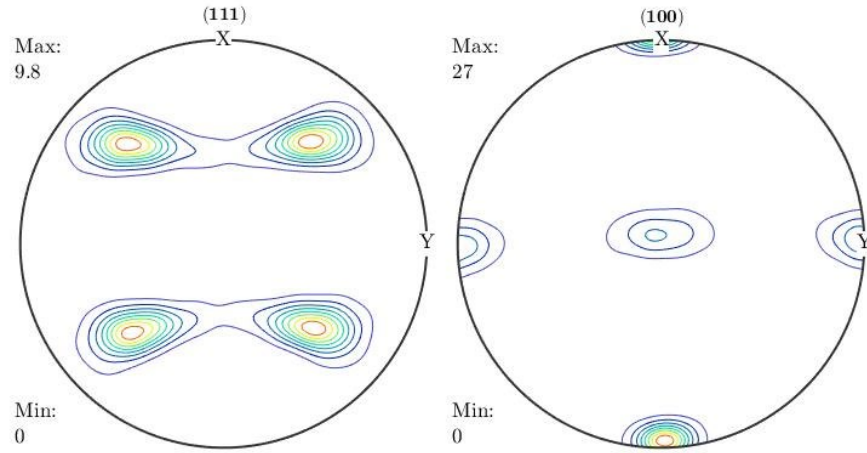
Figure 1: Pole figures of the initial texture of the extruded AA6060 alloy (after Khadyko et al. (2016) and Frodal et al. (2017)).

Uniaxial tensile tests in five directions of the extruded profile were performed to characterize the plastic anisotropy of the material (see Khadyko et al. (2016) for details). Owing to the presence of the strong recrystallization texture, the r-value variation with the orientation to the extrusion direction (ED) displays a minimum around 45° irrespective of the level of plastic strain, while the maximum r-value is at 90° to ED. The directional dependency of the normalized flow stresses and the r-values are shown in Figure 2 for a logarithmic plastic strain of 0.5 (experimental data based on Khadyko et al. (2016))[1].

It should be noted that the extruded AA6060 alloy used for parameter identification differed slightly from the extruded AA6060 alloy for which the uniaxial tensile behavior for smooth and notched specimens was reported by Khadyko et al. (2015). Nevertheless, the two extruded AA6060 alloys had both strong recrystallization texture and similar yield stress and hardening. Therefore, we do not consider this as being an issue. The main goal of this work is to demonstrate the capabilities of the Cazacu (2018) elastic-plastic model to capture the effect of specimen geometry (smooth or notched) on the shape of the deformed cross-section close to fracture. Since the material has a weak evolution in texture in uniaxial tension, its yield locus evolves in a way so that it can be calibrated based on experimental data at a certain plastic strain, and the anisotropy coefficients involved in the yield criterion can be taken constant.

---

[1] An error was detected in the calculation of the experimental r-values presented in Khadyko et al. (2016). The error has been corrected, and only the corrected data are used throughout this paper.

3. Polycrystal model based on a recent description of the single-crystal behavior

To generate additional information concerning the yield surface of the AA6060 alloy, we performed virtual tests using the recent polycrystal model of Chandola et al. (2017). The polycrystal is represented by a finite set of orientations, each one representing a given volume fraction chosen to reproduce the texture shown in Figure 1. Elastic deformations are neglected. The plastic behavior of the constituent crystals (or grains) is described using the new single crystal model of Cazacu et al. (2018). The plastic strain-rate deviator $\mathbf{D}^p$ of the polycrystal, expressed in the loading frame, is given as

$$\mathbf{D}^p = \frac{\dot{\lambda}}{N} \sum_{i=1}^{N} \mathbf{R}_i \frac{\partial \bar{\sigma}_{grain}^i \left(\mathbf{R}_i^T \boldsymbol{\sigma} \mathbf{R}_i \right)}{\partial \left(\mathbf{R}_i^T \boldsymbol{\sigma} \mathbf{R}_i \right)} \mathbf{R}_i^T \tag{1}$$

where $\dot{\lambda}$ is the plastic multiplier, $\boldsymbol{\sigma}$ denotes the applied stress tensor, N is the number of grains considered in the polycrystalline material, $\bar{\sigma}_{grain}^i$ is the effective stress of grain i, and $\mathbf{R}_i$ is the transformation matrix for passage from the crystal axes of grain i to the loading frame axes.

Let $Ox_1x_2x_3$ denote the Cartesian coordinate system associated with the crystal axes (i.e., the <100> crystal directions). In this coordinate system, the expression of the effective stress $\bar{\sigma}_{grain}$ is:

$$\bar{\sigma}_{grain} = \frac{3}{\left(27 - 4cn_1^2\right)^{1/6}} \left\{ \begin{bmatrix} \frac{1}{2}\left(\sigma_{11}'^2 + \sigma_{22}'^2 + \sigma_{33}'^2\right) + m_2\left(\sigma_{12}'^2 + \sigma_{13}'^2 + \sigma_{23}'^2\right) \end{bmatrix}^3 \\ -c\left[n_1\sigma_{11}'\sigma_{22}'\sigma_{33}' - n_3\left(\sigma_{33}'\sigma_{12}'^2 + \sigma_{11}'\sigma_{23}'^2 + \sigma_{22}'\sigma_{13}'^2\right) + 2n_4\sigma_{12}'\sigma_{13}'\sigma_{23}' \right]^2 \right\}^{1/6} \tag{2}$$

where m_2, n_1, n_3, n_4 are anisotropy coefficients and c is a parameter that describes the relative importance of the second-order and third-order cubic stress-invariants on yielding (for more details on the formulation and derivation of the expressions of the stress-invariants for the crystal classes of the cubic system, see Cazacu et al. (2018)). In Eq. (2), $\boldsymbol{\sigma}'$ denotes the Cauchy stress deviator, i.e., $\boldsymbol{\sigma}' = \boldsymbol{\sigma} - \sigma_m \mathbf{I}$ with $\sigma_m = \frac{1}{3}\text{tr}(\boldsymbol{\sigma})$, where $\mathbf{I}$ is the second-order identity tensor while "tr" denotes the trace operator. It is worth mentioning that the effective stress associated to the

single crystal model of Cazacu et al. (2018) is C^2 differentiable for any three-dimensional stress states (see Eq. (2)).

135   The mathematical form of the single-crystal criterion given by Eq. (2) was obtained using rigorous theorems of representation of tensor functions (see Smith and Rivlin (1958); Wang (1970) and I-Shih (1982)). Therefore, the properties of invariance of the yield function with respect to the intrinsic symmetries associated to single crystals belonging to the cubic system are automatically satisfied. Moreover, in this manner the minimum number of anisotropy
140   coefficients that ought to be involved in the formulation to satisfy both the condition of insensitivity of plastic deformation to hydrostatic pressure and the invariance requirements are obtained. For full mathematical proofs and a detailed presentation of the derivation of Eq. (2), the reader is referred to Cazacu et al. (2018).

The polycrystal model based on the single-crystal criterion given by Eq. (2) has previously been
145   applied to model the effect of different texture components on the polycrystalline behavior of textured aluminum and steel sheets (see Chandola et al. (2017, 2018)). In this paper, the polycrystal model will be used to generate yield loci for the extruded AA6060 alloy. In all the polycrystal model results presented hereafter, we used 2612 predominant grain orientations to represent the texture given in Figure 1. Calibration of the parameters involved in the model, i.e.,
150   the anisotropy coefficients m_2, n_1, n_3, n_4 and c, is done based on the yield stress ratios and r-values in five different orientations θ with respect to ED for smooth specimens. The parametrization obtained for the single crystal model is: $m_2 = 0.50$, $n_1 = 1.31$, $n_3 = 0.52$, $n_4 = 1.2$ and $c = 0.57$. The yield stress ratios and r-values for a logarithmic plastic strain of 0.5 were used in the parameter identification in an attempt to account for the influence of large deformation on
155   the plastic anisotropy. Recall that the main aim of the study is to investigate whether the macroscopic elastic-plastic model can predict the shape of the deformed cross-section of the tensile specimens close to fracture.

Let us define Oxyz, the Cartesian coordinate system associated with the orthotropy axes of the AA6060 alloy, where the x axis is along the extrusion direction (ED). As it is customary, we
160   denote σ_θ the uniaxial tensile flow stress while r_θ is the r-value (or Lankford coefficient), i.e., the ratio between the transverse and thickness strain-rates, respectively.
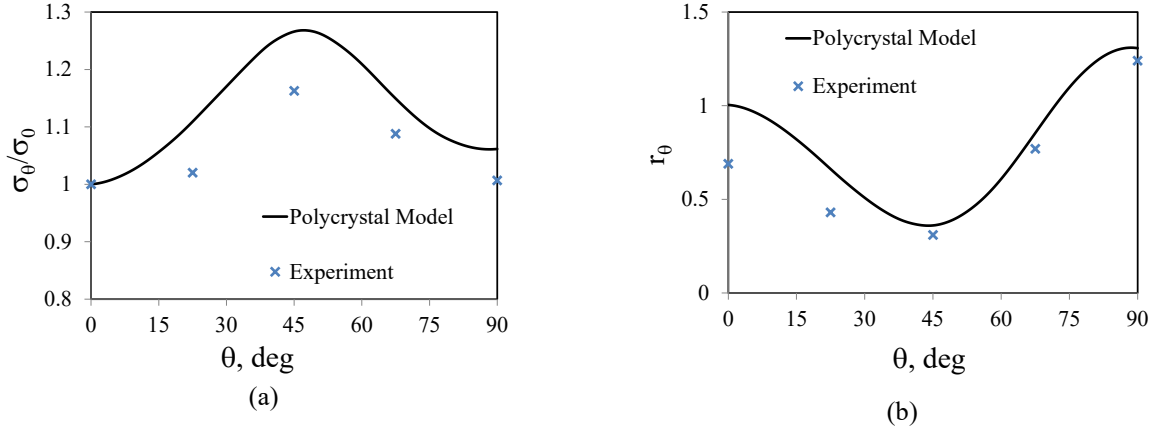
6

Figure 2: Predicted anisotropy for the AA6060 alloy according to the polycrystal model given by Eqs. (1)-(2): (a) Uniaxial tensile flow stresses, and (b) r-values. The stresses in (a) are normalized by the flow stress along ED. Experimental data at a logarithmic plastic strain of 0.5.

The polycrystal model predictions of the anisotropy in flow stresses and plastic strain-rate ratios (or r-values) of the AA6060 alloy are shown in Figure 2 (solid line) together with the experimental data (symbols). Note that the polycrystal model captures well the experimental trends (see Figure 2). Moreover, the polycrystal model predicts correctly the effect of the dominance of the cube component on the macroscopic mechanical properties, namely that extrema in the variation of $\sigma_\theta = \sigma(\theta)$ and $r_\theta = r(\theta)$ with the loading orientation θ are at 0°, ~45°, and 90°, while also capturing the influence of the minor Goss component which leads to an $r(90°) = 1.26$ for the AA6060 alloy instead of $r(90°) = 1$ for a pure cube texture. Indeed, it is also worth mentioning that for the pure cube texture component (which is the dominant component for the extruded AA6060), using Eq. (2), analytical formulas for the evolution of the uniaxial yield stresses σ_θ and r_θ with the loading orientation θ were deduced in Cazacu et al. (2019). It was also shown that irrespective of the parametrization, the model predicts $\sigma(\theta) = \sigma(90° - \theta)$ and $r(\theta) = r(90° - \theta)$, with extrema at 0°, 45°, and 90°, and $r(0°) = r(90°) = 1$. On the other hand, for the pure Goss component (which is a minor component for the polycrystalline AA6060), it can be analytically deduced that $r(0°) = 1$ irrespective of the value of the material parameters, while $r(90°)$ depends on the

7

parametrization. For example, for $m_2 = 0.5$, $n_1 = 1.31$, $n_3 = 0.52$, $n_4 = 1.2$, $c = 0.57$ for pure

Goss texture, one obtains: $r(90°) = 5.35$.

In summary, the polycrystal model based on the single crystal criterion given by Eq. (2) predicts correctly the influence of the dominant texture component while accounting for the presence of the minor component. Figure 3 shows the projection of the AA6060 yield surface in the $(\sigma_{xx}, \sigma_{yy})$ plane for several fixed levels of the shear stress (σ_{xy} / σ_0 = 0, 0.2, 0.4) obtained with the polycrystal model.
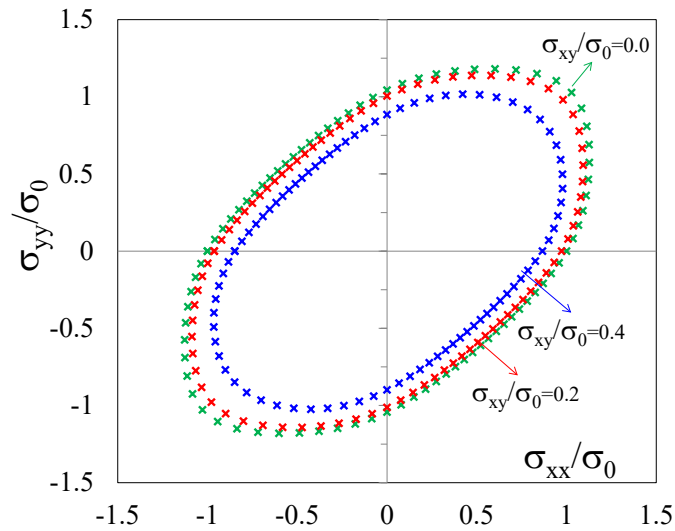

Figure 3: Predicted isocontours of the yield surface of the AA6060 alloy corresponding to σ_{xy} / σ_0 = 0, 0.2, and 0.4 in the $(\sigma_{xx}, \sigma_{yy})$ plane according to the polycrystal model given by Eqs. (1)-(2). The *x,y* axes are along the extrusion and transverse directions, respectively. Stresses are normalized by the yield stress along the extrusion direction σ_0.

8

4. Macroscopic elastic-plastic model with the Cazacu (2018) orthotropic yield criterion

In view of structural applications, a macroscopic level model that captures the key physics and can be easily implemented in an FE framework for further use in large-scale simulations is desirable. As mentioned, in this paper a macroscopic level elastic-plastic model based on the Cazacu (2018) orthotropic yield criterion will be used. The constitutive assumptions and the identification procedure based on the available mechanical and numerical data obtained with the polycrystal model are presented in the following.

4.1 Governing equations

The total rate of deformation $\mathbf{D}$ is the sum of an elastic part and a plastic part $\mathbf{D}^p$. The hypoelastic response is described as

$$\dot{\boldsymbol{\sigma}} = \mathbf{C}^e : \left(\mathbf{D} - \mathbf{D}^p \right) \tag{3}$$

where $\dot{\boldsymbol{\sigma}}$ is an objective rate of the Cauchy stress tensor $\boldsymbol{\sigma}$ (see Green and Naghdi (1965) and Abaqus, 2014), $\mathbf{C}^e$ is the fourth-order stiffness tensor, while ":" denotes the double contracted product between the two tensors. In this work, we assume linear elastic isotropy, so, with respect to any coordinate system, $\mathbf{C}^e$ is given as

$$C_{ijkl}^e = G\left(\delta_{ik}\delta_{jl} + \delta_{il}\delta_{jk} \right) + \left(K - \frac{2}{3}G \right)\delta_{ij}\delta_{kl} \tag{4}$$

with $i,j,k,l = 1...3$, δ_{ij} is the Kronecker delta, while G and K are constants which denote the shear and bulk modulus, respectively.

To account for the anisotropic plastic behavior of the AA6060 alloy, yielding is described with the Cazacu (2018)'s orthotropic yield criterion. This criterion is the orthotropic extension of an isotropic yield criterion which is homogeneous of degree 8 in stresses. As it has been amply discussed in literature, yield functions which are homogeneous of degree 8 in stresses offer more flexibility in describing the behavior of certain polycrystalline FCC materials (e.g. see Hosford (1972)). Cazacu (2018)) orthotropic yield criterion is expressed as:

$$F\left(J_2^0, J_3^0 \right) = \left(J_2^0 \right)^4 - \alpha \left(J_2^0 \right)\left(J_3^0 \right)^2 \tag{5}$$

In Eq.(5), α is a material parameter, and J_2^0, J_3^0 are orthotropic stress invariants. The expressions of J_2^0, J_3^0 relative to a corotational coordinate system (x, y, z) associated with the orthotropy axes of the material are given by (see Cazacu and Barlat (2001) for details)

$$J_2^0 = \frac{a_1}{6}\left(\sigma_{xx} - \sigma_{yy}\right)^2 + \frac{a_2}{6}\left(\sigma_{yy} - \sigma_{zz}\right)^2 + \frac{a_3}{6}\left(\sigma_{xx} - \sigma_{zz}\right)^2 + a_4\sigma_{xy}^2 + a_5\sigma_{xz}^2 + a_6\sigma_{yz}^2 \tag{6}$$

and

$$
\begin{aligned}
J_3^0 &= \frac{1}{27}(b_1 + b_2)\sigma_{xx}^3 + \frac{1}{27}(b_3 + b_4)\sigma_{yy}^3 + \frac{1}{27}\left[2(b_1 + b_4) - b_2 - b_3\right]\sigma_{zz}^3 \\
&\quad - \frac{1}{9}\left(b_1\sigma_{yy} + b_2\,\sigma_{zz}\right)\sigma_{xx}^2 - \frac{1}{9}(b_3\sigma_{zz} + b_4\,\sigma_{xx})\sigma_{yy}^2 \\
&\quad - \frac{1}{9}\left[(b_1 - b_2 + b_4)\sigma_{xx} + (b_1 - b_3 + b_4)\,\sigma_{yy}\right]\sigma_{zz}^2 \\
&\quad + \frac{2}{9}(b_1 + b_4)\,\sigma_{xx}\,\sigma_{zz}\sigma_{yy} - \frac{\sigma_{xz}^2}{3}\left[2b_9\,\sigma_{yy} - b_8\,\sigma_{zz} - (2b_9 - b_8)\sigma_{xx}\right] \\
&\quad - \frac{\sigma_{xy}^2}{3}\left[2b_{10}\,\sigma_{zz} - b_5\sigma_{yy} - (2b_{10} - b_5)\sigma_{xx}\right] - \frac{\sigma_{yz}^2}{3}\left[(b_6 + b_7)\sigma_{xx} - b_6\sigma_{yy} - b_7\sigma_{zz}\right] \\
&\quad + 2b_{11}\sigma_{xy}\sigma_{xz}\sigma_{yz}
\end{aligned}
\tag{7}
$$

In Eqs. (6)-(7), a_i $(i = 1...6)$ and b_k $(k = 1...11)$ are constants. The stress invariant J_2^0 is a homogenous polynomial of degree two in stresses, insensitive to hydrostatic pressure (i.e., $J_2^0(\boldsymbol{\sigma} + p\mathbf{I}) = J_2^0(\boldsymbol{\sigma})$ for any $\boldsymbol{\sigma}$ and p), and respects orthotropic symmetries. The stress invariant J_3^0 is a homogenous third-order polynomial in stresses, which is pressure-insensitive, and it is invariant to any transformation belonging to the orthotropy group. For more details concerning the derivation of the expressions of these orthotropic invariants, see Cazacu and Barlat (2001) and the book of Cazacu et al. (2019).

If all $a_i = 1$ and $b_k = 1$, $J_2^0 = J_2$ and $J_3^0 = J_3$ (see Eq. (6)-(7)), where $J_2 = \mathrm{tr}(\boldsymbol{\sigma}'^2)/2$ and $J_3 = \mathrm{tr}(\boldsymbol{\sigma}'^3)/3$ are the isotropic invariants of the stress deviator. Therefore, the isotropic form Cazacu (2018) reduces to

$$\bar{\sigma} = m \left[\left(J_2^0 \right)^4 - \alpha \left(J_2^0 \right) \left(J_3^0 \right)^2 \right]^{1/8} \tag{8}$$

235 In the above equation, m is a constant defined such that for uniaxial tension in the x-direction the effective stress reduces to the yield stress, i.e.,

$$m = \frac{3\sqrt{2}}{\left\{ \left[27 \left(a_1 + a_3 \right)^3 - 8\alpha \left(b_1 + b_2 \right)^2 \right] \left(3a_1 + 3a_3 \right) \right\}^{1/8}} \tag{9}$$

Invoking the associated flow rule, the plastic part of the rate of deformation tensor $\mathbf{D}^p$ is given by

$$\mathbf{D}^p = \dot{\lambda} \frac{\partial \bar{\sigma}}{\partial \boldsymbol{\sigma}} \tag{10}$$

where $\dot{\lambda} \geq 0$ is the plastic multiplier, and the effective stress, $\bar{\sigma}$, is given by Eq. (8).

240 The hardening is assumed isotropic and governed by the equivalent plastic strain. Specifically,

$$\bar{\sigma} = Y(\bar{\varepsilon}_p),$$

with $\bar{\sigma}$ given by Eq. (8) and $Y(\bar{\varepsilon}_p)$ being defined by a Swift-type hardening law, i.e.:

$$Y\left(\bar{\varepsilon}^p \right) = C_1 \left(C_2 + \bar{\varepsilon}_p \right)^n \tag{11}$$

where C_1, C_2 and n are constants, while $\bar{\varepsilon}_p$ is the work-equivalent plastic strain associated to the effective stress $\bar{\sigma}$.

245 The elastic-plastic model given by Eqs. (3)-(11) was implemented in the commercial FE code Abaqus (see Abaqus, 2009). For this purpose, a user material subroutine (UMAT) was developed for the implicit solver, i.e., Abaqus/Standard. A fully implicit integration algorithm was used for solving the governing equations. Thus, it is ensured that the equilibrium equations are satisfied at each time-step. The choice of objective stress rate is not significant for isotropic hardening (see

250 Hughes (1984)), which is the case considered here. Nevertheless, the objective stress rates used in the commercial FE code ABAQUS are either Jaumann or Green-Naghdi rates (depending on the type of FE elements, see Abaqus, 2014) while the material frame is updated based on the orthogonal rotation tensor $\mathbf{R}$ (the rotation tensor is derived from the polar decomposition of the deformation gradient $\mathbf{F} = \mathbf{RU}$, with $\mathbf{U}$ the right stretch tensor).

11

4.2 Parameter identification for the AA6060 alloy

For general 3-D stress conditions the orthotropic criterion of Cazacu (2018) involves 17 independent anisotropy coefficients (for proof see Cazacu (2018)). Calibration of the orthotropic criterion was done using the numerical yield stresses obtained with the polycrystal model given by Eqs. (1)-(2) (see also Figure 3) and the available experimental flow stresses and plastic strain-rate ratios in conjunction with the following equations for the normalized uniaxial flow stresses σ_θ / σ_0 and r-values, r_θ:

$$\frac{\sigma_\theta}{\sigma_0} = \frac{1}{m} \left\{ \begin{bmatrix} \left(a_1/6 + a_3/6\right)\cos^4\theta + \left(a_4 - a_1/3\right)\cos^2\theta\sin^2\theta + \left(a_1/6 + a_2/6\right)\sin^4\theta \end{bmatrix}^4 \\ -\alpha \begin{bmatrix} \cos^6\theta\left(b_1 + b_2\right)/27 + \sin^6\theta\left(b_3 + b_4\right)/27 \\ -\sin^2\theta\cos^4\theta\left(b_1 + 3b_5 - 6b_{10}\right)/9 \\ -\sin^4\theta\cos^2\theta\left(b_4 - 3b_5\right)/9 \end{bmatrix}^2 \begin{bmatrix} \left(a_1/6 + a_3/6\right)\cos^4\theta \\ +\left(a_4 - a_1/3\right)\cos^2\theta\sin^2\theta \\ +\left(a_1/6 + a_2/6\right)\sin^4\theta \end{bmatrix} \right\}^{-1/8} \tag{12}$$

and

$$r_\theta = -\frac{\dfrac{\partial\overline{\sigma}}{\partial\sigma_{xx}}\left(\sin^2\theta\right) - \sin2\theta\dfrac{\partial\overline{\sigma}}{\partial\sigma_{xy}} + \dfrac{\partial\overline{\sigma}}{\partial\sigma_{yy}}\left(\cos^2\theta\right)}{\dfrac{\partial\overline{\sigma}}{\partial\sigma_{xx}} + \dfrac{\partial\overline{\sigma}}{\partial\sigma_{yy}}} \tag{13}$$

with

$$\frac{\partial\overline{\sigma}}{\partial\sigma_{ij}} = \frac{m}{8}\left\{\left[4\left(J_2^0\right)^3 - \alpha\left(J_3^0\right)^2\right]\frac{\partial J_2^0}{\partial\sigma_{ij}} - 2\alpha\left(J_3^0\right)\left(J_2^0\right)\frac{\partial J_3^0}{\partial\sigma_{ij}}\right\}\left[\left(J_2^0\right)^4 - \alpha\left(J_2^0\right)\left(J_3^0\right)^2\right]^{-\frac{7}{8}} \tag{14}$$

for $i, j = 1...3$. The expressions of the derivatives of the orthotropic invariants J_2^0 and J_3^0 are given in Appendix 1.

Comparisons between the theoretical flow stresses and r-values according to the criterion of Cazacu (2018) and the experimental data are given in Figure 4. Note that with the Cazacu (2018) criterion, it is possible to capture that the AA6060 alloy has $r(0) < 1$. This is a direct consequence of the criterion accounting for orthotropic symmetry. As already mentioned, the polycrystal model also describes well the anisotropy in r-values of this alloy (see Figure 2(b)). However, given that the dominant texture components are cube and Goss, the predicted value for $r(0)$ is close to 1 (due to cubic symmetries, for both ideal cube texture and Goss texture:

12

$r(0)=1$). As concerns the anisotropy in yield stresses, both models describe correctly the experimental trends (see Figure 2(a) and Figure 4(a)). Isocontours of the yield surface for the material in the plane $\left(\sigma_{xx}, \sigma_{yy}\right)$ for several fixed levels σ_{xy}/σ_0 = 0, 0.2, and 0.4 and the numerical yield points obtained with the polycrystal model (see Section 3) are given in Figure 5. The corresponding numerical values of the anisotropy coefficients are given in Table 1. Note that there is a good agreement between the model and the mechanical and numerical data.

(a)   (b)
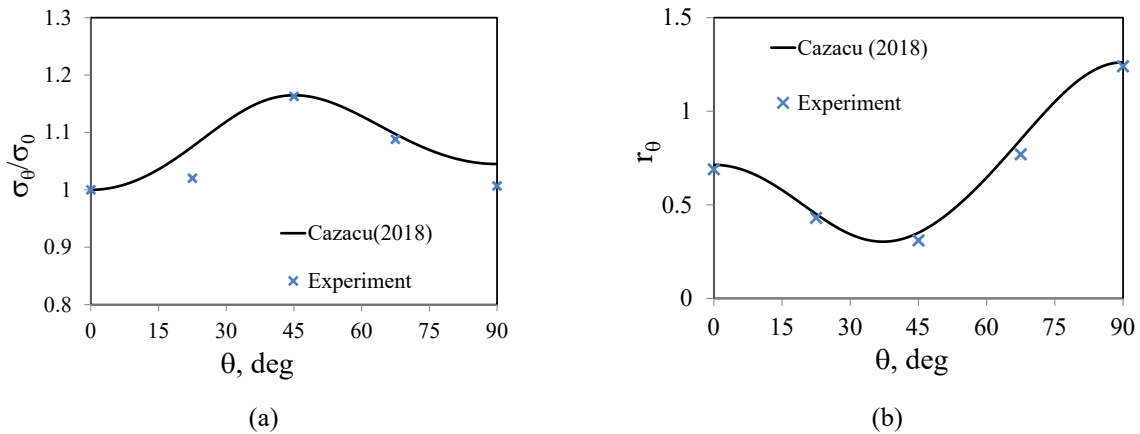
Figure 4: Predicted anisotropy of the AA6060 alloy according to the orthotropic criterion of Cazacu (2018), Eq. (5): (a) evolution of the tensile flow stress with the tensile direction and (b) plastic strain-rate ratios (r-values). Experimental data at a logarithmic plastic strain of 0.5
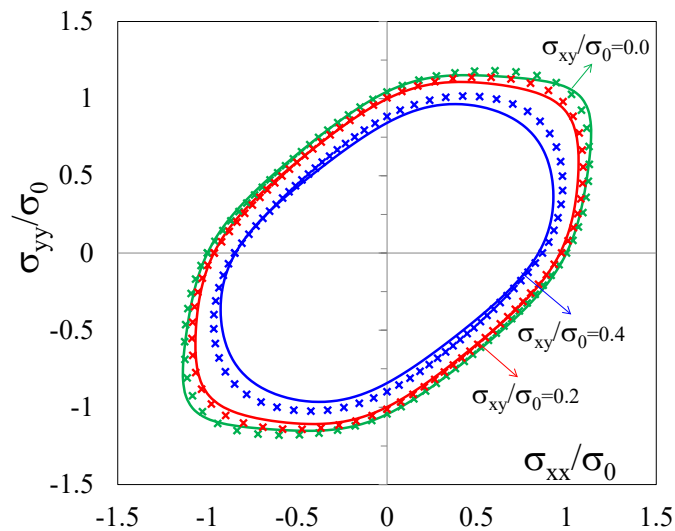

Figure 5: Iso-contours of the yield surface of the AA6060 alloy according to the orthotropic criterion of Cazacu (2018) and numerical yield points obtained with the polycrystal model given

13

285   by Eqs. (1)-(2) (symbols) corresponding to $\sigma_{xy}/\sigma_0 = 0, 0.2, 0.4$, respectively. The x, y axes are along the extrusion and transverse directions, respectively. Stresses are normalized by the yield stress in the extrusion direction.

The parameters involved in the hardening law given by Eq. (11) were determined using the Bridgman corrected experimental stress-strain curve obtained from a uniaxial tension test on a

290   smooth specimen with the loading axis along the extrusion direction reported by Khadyko et al. (2015) (see Figure 6). The numerical values are $C_1 = 243.6$ MPa, $C_2 = 0.011$ and $n = 0.187$.
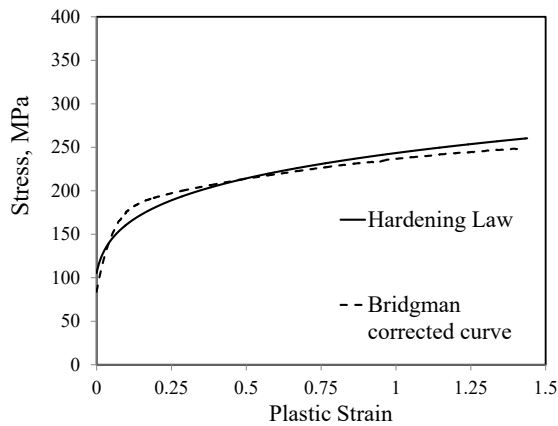
Figure 6: Bridgman corrected stress-strain curve used for calibration of the Swift hardening law (Eq. (11)) for the extruded AA6060 alloy from Khadyko et al. (2015). The loading axis is along

295   the extrusion direction.

Table 1: Anisotropy coefficients for the orthotropic criterion of Cazacu (2018) for the extruded AA6060 alloy.

Parameter	a_1	a_2	a_3	a_4	a_5	a_6	b_1	b_2	b_3
Values	1	0.978	1.094	0.713	1.002	1.002	2.00	0.538	1.839

	b_4	b_5	b_6	b_7	b_8	b_9	b_{10}	b_{11}	α
	0.960	0.665	1.002	1.002	1.002	1.002	1.079	1.50	0.999

300   The elastic parameters for the AA6060 alloy are taken as: $K = 66.67$ GPa and $G = 25.56$ GPa.

As mentioned, the tension test results conducted by Khadyko et al. (2015) on the AA6060 alloy using cylindrical specimens with the loading axis along the extrusion direction revealed that the post-test cross-sections are not elliptical. In the next section, the capability of the elastic-plastic

model with yielding according to the orthotropic Cazacu (2018) criterion to describe the large-strain behavior and the unusual post-test shapes of the cross-sections of the smooth and notched specimens is assessed.

5. Finite element simulations of tension tests

The same numerical values for the parameters of the Cazacu (2018) criterion and hardening law (see Table 1) were used in all F.E simulations. The specimen geometries and the FE meshes used in the simulations are shown in Figures 7-9. Note that since the cylindrical specimens were oriented along the axes of symmetry of the material, namely that the loading axis is along ED while TD (transverse direction) and ND (normal direction) are in the directions of the specimens' cross-section, symmetric boundary conditions can be applied. Therefore, only one-eighth of the specimens needs to be analyzed. The smooth specimen was meshed with 9000 linear three-dimensional eight-nodes reduced-integration element (C3D8R) in Abaqus/Standard (see Figure 7). The initial size of the elements along the axis of the specimen in the central cross-section is of 15 μm. The FE meshes for the 2 mm notch and the 0.8 mm notch specimens consisted of 8326 and 9984 C3D8R elements, respectively (see Figures 8-9). The mesh size has been adapted to ensure an accurate description of the necking zone (i.e., much larger concentration of elements was used close to the mid-section of the specimens, the zone undergoing severe plastic strains). Kinematic boundary conditions were imposed to all the nodes located at the upper surface of the specimen. Specifically, an axial displacement of 6.65 mm, 1.1 mm and 1.07 mm were applied at the end of the smooth specimen, the 2 mm notch and the 0.8 mm notch specimens, respectively. In all the F.E. simulations, the maximum time increment was fixed to $\Delta t = 10^{-3}$ s. Between four and seven iterations per increment were necessary for convergence in the return mapping algorithm, the tolerance in satisfying the yield criterion being 10^{-7} (0.1 Pa).

The enhanced hourglass control approach available in Abaqus/Standard was used for all the simulations. With this control method, element hourglassing did not occur in any simulation. In addition, the artificial energy due to the hourglass control was checked for all the simulations, and it was found negligible.

15

All simulations were run on a PC using one processor (Intel Core i7-4770, one core, 16 GB RAM). The CPU time for the simulations varied between around 1.5 hour for the smooth specimen and 2 hours for the notched specimens. A mesh-sensitivity study was also performed. It was found that further refinement of the mesh did not change the results (see Appendix 3).
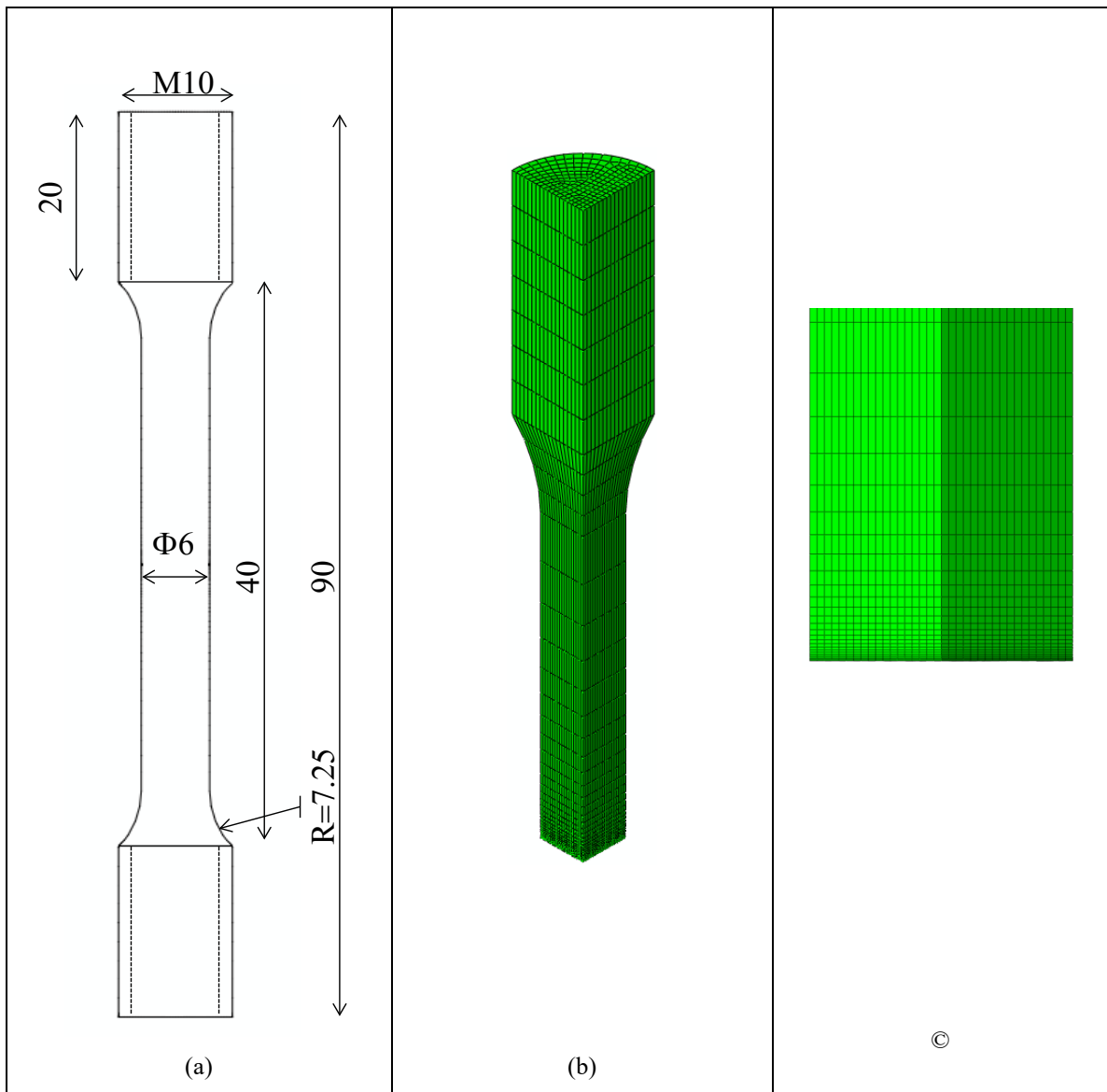

Figure 7: (a) Geometry of the cylindrical smooth tensile specimen; (b) FE mesh and (c) zoom of the central zone. The axis of the specimen is along the ED direction.
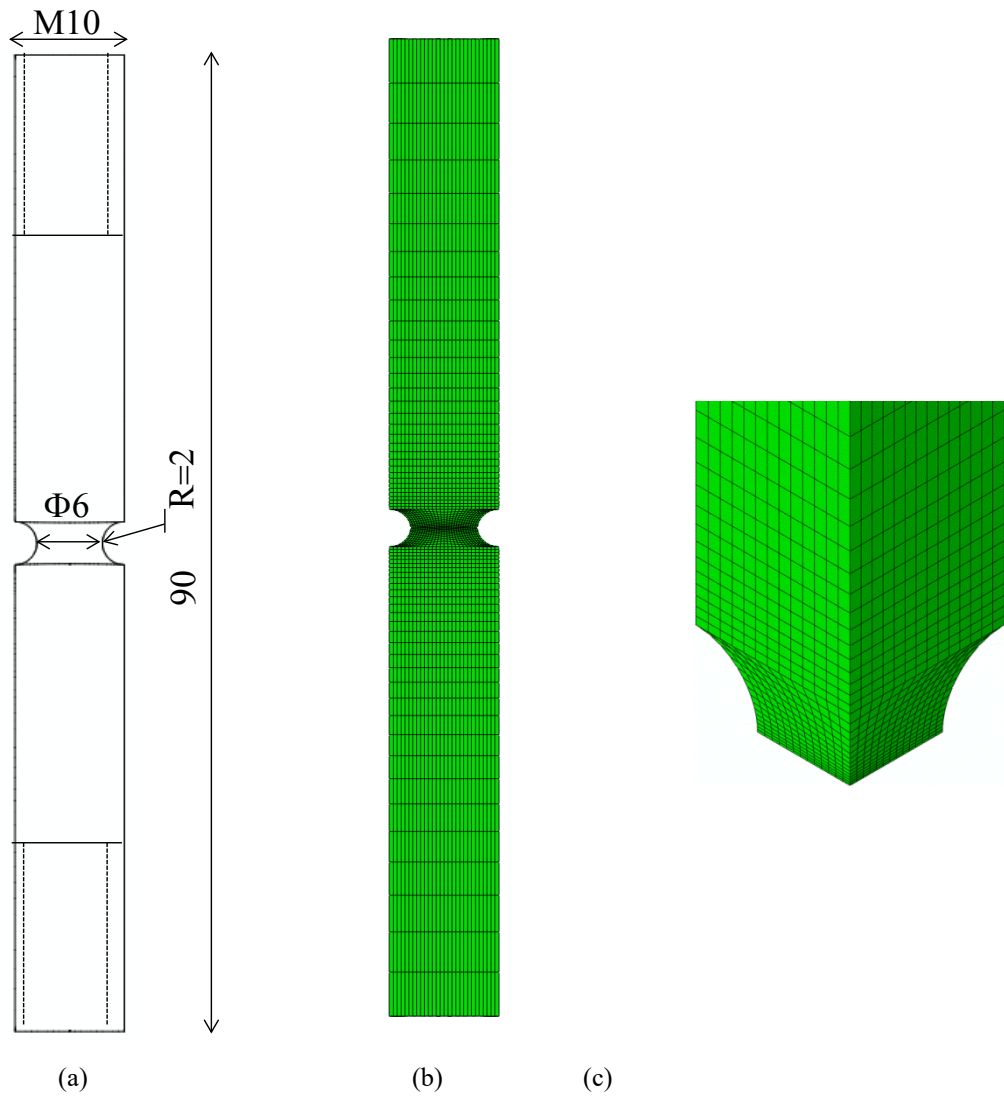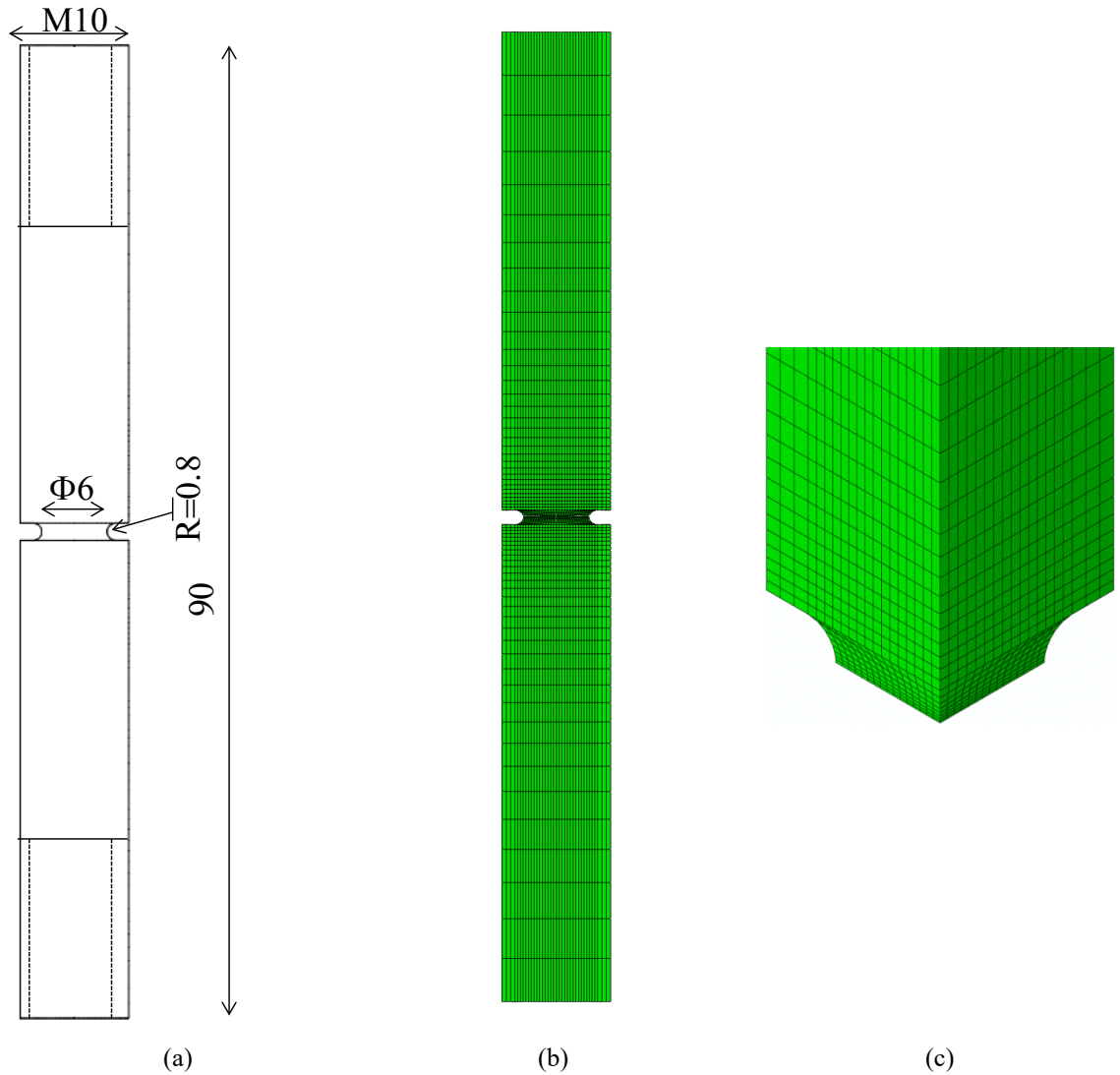
Figure 8: (a) Geometry of the 2 mm notched tensile specimen, (b) FE mesh and (c) zoom of the notched zone. The axis of the specimen is along the ED direction.

Figure 9: (a) Geometry of the 0.8 mm notched tensile specimen, (b) FE mesh and (c) zoom of the notched zone. The axis of the specimen is along the ED direction (*x*-direction).

The focus of our investigation is on the prediction of the effect of anisotropy on the material behavior, namely the difference between the shapes of the smooth and notched specimen cross-sections. While the values of the hardening parameters strongly influence the predicted force vs. diameter (see Appendix 2), their influence on the shapes of the cross-sections remains negligible. This is because the geometry of the cross-section is dictated by the material anisotropy.

355   Figure 10 shows the predicted isocontours of the equivalent plastic strain (associated to the effective stress given by Eq. (8)) in the minimum cross-section for the same levels of deformation observed experimentally for the smooth, 2 mm notch, and 0.8 mm notch specimens. Note that for the smooth specimen, the model predicts an elliptical cross-section. The deformation is homogeneous up to necking and as such the geometry of the cross-section can be

360   correlated to the anisotropy of the material, i.e., the material deforms more in the ND (z-direction) than in the TD (y-direction) direction (as observed from the measurements of the diameters along TD and ND throughout the experimental tests, see also Table 2). On the other hand, for the notched specimens where the deformation is no longer homogeneous, the model correctly predicts that the shape of the deformed cross-section depends on the specimen

365   geometry. Distinct rhomboid and rectangular shapes are predicted, in agreement with the experimental observations. To enable comparison with the experimental cross-sections, the FE predictions obtained with the macroscopic elastic-plastic model (interrupted lines) have been superposed on the micrographs of the cross-sections of the specimens (i.e., the fracture surfaces) in Figure 10. It is worth noting that for both the smooth and notched specimens, the FE

370   predictions of the geometry of the respective cross-sections are in good agreement with the experimental data. When analyzing the results, note that in the micrograph of the final cross-section of the 2 mm notch specimen, the orthotropy axes of the material (i.e., the TD and ND axes) are rotated. Thus, in order to match the orientation of the anisotropy axes in the micrograph when superposing the FE points, we had to rotate the simulated cross-section of the 2 mm

375   specimen as well (see Figure 10).

19

(a) Smooth specimen

(b) 2 mm notched specimen

(c) 0.8 mm notched specimen
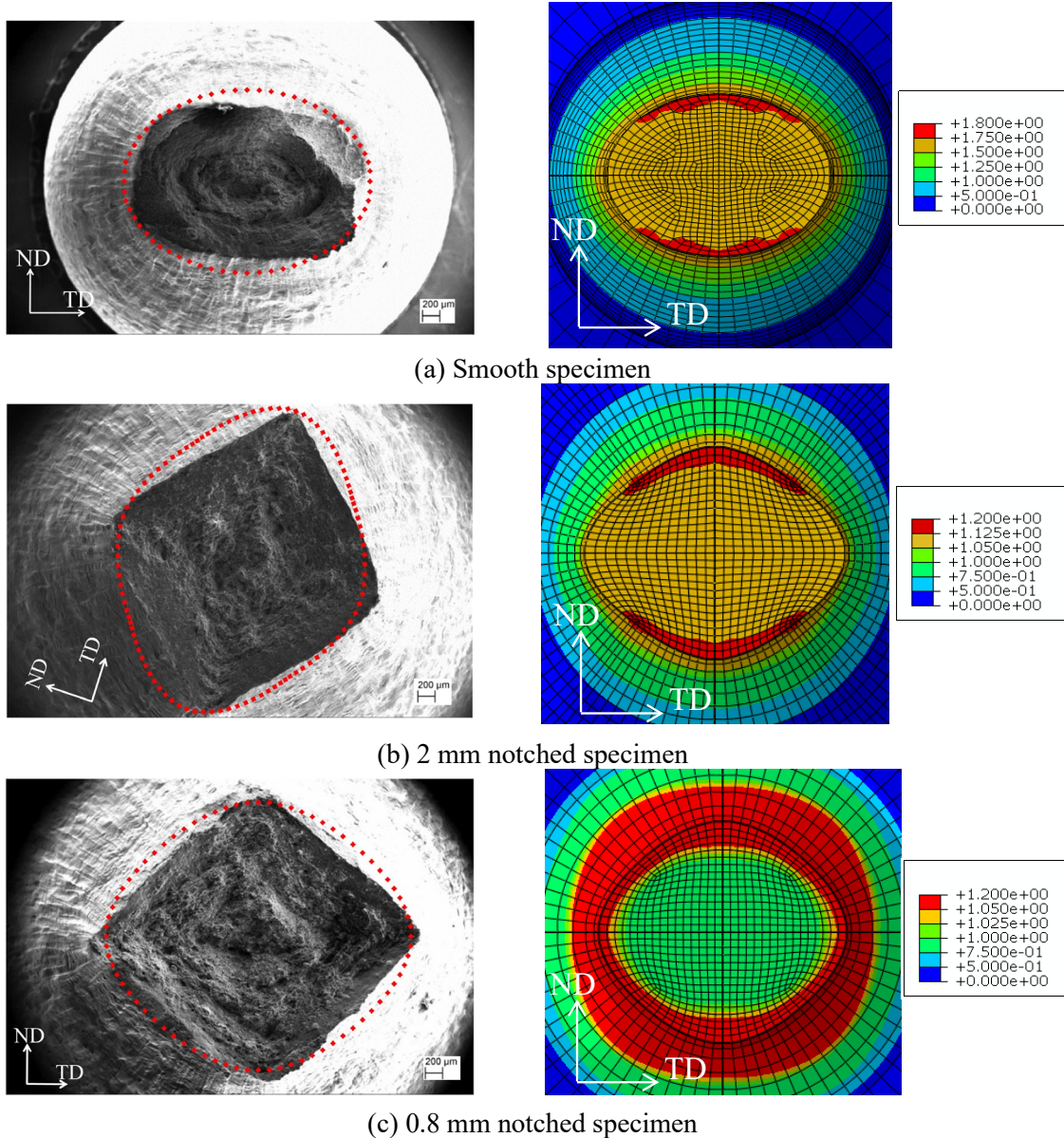
Figure 10: Predicted isocontours of the equivalent plastic strain (associated to the effective stress given by Eq. (8)) in the minimum cross-section (right) for the same levels of deformation observed experimentally (after Khadyko et al. (2015)) and micrographs of the cross-sections (left) for (a) smooth specimen (b) 2 mm notched specimen and (c) 0.8 mm notched specimen. The FE predictions (red dots) are superposed on the micrographs of the specimens.

To allow for a quantitative comparison, the predicted diameter along the TD and ND directions of the final cross-sections for each specimen are given in Table 2. The good agreement between the experimental and simulated ratio of the diameters should be noted.

20

385

Table 2: Predicted versus experimental diameters of the cross-section along ND and TD for the smooth and notched specimens.

Specimen Type	Smooth	2 mm notch	0.8 mm notch
Diameter along TD (mm)			
Experimental	2.97	4.07	4.11
Simulations	3.06	4.02	4.04
Diameter along ND (mm)			
Experimental	2.04	3.51	3.63
Simulations	2.18	3.29	3.61
Ratio of diameters (TD/ND)			
Experimental	1.46	1.16	1.13
Simulations	1.40	1.22	1.12

Conclusions

390 The unusual deformation of a strongly textured AA6060 alloy when subjected to uniaxial tension loading was predicted using the orthotropic Cazacu (2018) yield criterion. This yield criterion is able to capture the difference in the shape of the cross-section between smooth and notched specimens. Specifically, for the smooth specimen with its axis along the extrusion direction, the

395 minimum cross-section evolves from a circle to an ellipse, the predicted diameters of the final cross-section being in good agreement with the measured values. For the notched specimens with their axis along the extrusion direction, the minimum cross-section evolves from a circular shape to an approximately rectangular, or rhomboidal shape, respectively as observed in the experiments.

400 Due to the limited mechanical data available, the experimental database for the identification of the Cazacu (2018) orthotropic criterion has been populated with numerical data obtained with virtual testing. Yield points have been determined using the polycrystalline model of Chandola et al. (2017). The main feature of this polycrystal model is the use of the single crystal criterion of Cazacu et al. (2018) for cubic materials.

405 Comparisons between FE simulations and experimental tests on both smooth and notched axisymmetric specimens (notch size of 0.8mm and 2mm) show that the Cazacu (2018) criterion predicts correctly the deformation characteristics of the extruded AA6060 alloy. It is also worth mentioning that beside the good agreement between experiments and simulation results, the use

of the orthotropic Cazacu (2018) criterion enables simulation for large-scale applications in considerably less time than CP-FE simulations.

The key objective of this paper was modeling the effect of notch geometry on the deformation of a strongly anisotropic material subject to uniaxial tension. Modeling of shear or cyclic loadings would require consideration of an orthotropic criterion in conjunction with anisotropic hardening.

Appendix 1: Derivatives of the orthotropic invariants

The partial derivatives of the orthotropic third-invariant J_2^0 are expressed as

$$\frac{\partial J_2^0}{\partial \sigma_{xx}} = \left(a_1 + a_3\right)\sigma_{xx}/3 - a_1\sigma_{yy}/3 - a_3\sigma_{zz}/3$$

$$\frac{\partial J_2^0}{\partial \sigma_{yy}} = -a_1\sigma_{xx}/3 + \left(a_1 + a_2\right)\sigma_{yy}/3 - a_2\sigma_{zz}/3$$

$$\frac{\partial J_2^0}{\partial \sigma_{zz}} = -a_3\sigma_{xx}/3 - a_2\sigma_{yy}/3 + \left(a_3 + a_2\right)\sigma_{zz}/3 \qquad (A.1)$$

$$\frac{\partial J_2^0}{\partial \sigma_{yz}} = a_6\sigma_{yz}, \quad \frac{\partial J_2^0}{\partial \sigma_{xz}} = a_5\sigma_{xz}, \quad \frac{\partial J_2^0}{\partial \sigma_{xy}} = a_4\sigma_{xy}$$

The partial derivatives of the orthotropic third-invariant J_3^0 are expressed as:

22

$$\frac{\partial J_3^0}{\partial \sigma_{xx}} = \frac{b_1}{9}\left(\sigma_{xx} - \sigma_{yy}\right)^2 + \frac{b_2}{9}\left(\sigma_{xx} - \sigma_{zz}\right)^2 - \frac{b_1 + b_4}{9}\left(\sigma_{yy} - \sigma_{zz}\right)^2$$

$$- \frac{1}{3}\left[\left(b_6 + b_7\right)\sigma_{yz}^2 - \left(2b_9 - b_8\right)\sigma_{xz}^2 - \left(2b_{10} - b_5\right)\sigma_{xy}^2\right]$$

$$\frac{\partial J_3^0}{\partial \sigma_{yy}} = \frac{b_4}{9}\left(\sigma_{xx} - \sigma_{yy}\right)^2 - \frac{b_1 + b_4}{9}\left(\sigma_{xx} - \sigma_{zz}\right)^2 + \frac{b_3}{9}\left(\sigma_{yy} - \sigma_{zz}\right)^2$$

$$- \frac{1}{3}\left[2b_9\,\sigma_{xz}^2 - b_5\sigma_{xy}^2 - b_6\sigma_{yz}^2\right]$$

$$\frac{\partial J_3^0}{\partial \sigma_{zz}} = -\frac{\partial J_3^0}{\partial \sigma_{xx}} - \frac{\partial J_3^0}{\partial \sigma_{yy}}$$

$$\frac{\partial J_3^0}{\partial \sigma_{yz}} = -\frac{\sigma_{yz}}{3}\left[\left(b_6 + b_7\right)\sigma_{xx} - b_6\sigma_{yy} - b_7\sigma_{zz}\right] + b_{11}\sigma_{xy}\sigma_{xz}$$

$$\frac{\partial J_3^0}{\partial \sigma_{xz}} = -\frac{\sigma_{xz}}{3}\left[2b_9\,\sigma_{yy} - b_8\,\sigma_{zz} - \left(2b_9 - b_8\right)\sigma_{xx}\right] + b_{11}\sigma_{xy}\sigma_{yz}$$

$$\frac{\partial J_3^0}{\partial \sigma_{xy}} = -\frac{\sigma_{xy}}{3}\left[2b_{10}\,\sigma_{zz} - b_5\sigma_{yy} - \left(2b_{10} - b_5\right)\sigma_{xx}\right] + b_{11}\sigma_{xz}\sigma_{yz} \qquad (A.2)$$

Note that for isotropy, i.e. each of the constants $a_i = 1\,(i = 1...6)$ and if each of the constants $b_k = 1\,(k = 1...11)$, we have:

$$\frac{\partial J_2^0}{\partial \sigma_{ij}} = \frac{\partial J_2}{\partial \sigma_{ij}} = \sigma'_{ij}, \quad \frac{\partial J_3^0}{\partial \sigma_{ij}} = \frac{\partial J_3}{\partial \sigma_{ij}} = \left(\sigma'^2\right)_{ij} - \frac{2}{3}J_2\delta_{ij} \qquad (A.3)$$

430

Appendix 2: Influence of hardening parameters on the response

The FE results presented in Fig. 10 were obtained using the isotropic hardening law given by Eq. (11) with $C_1 = 243.6$ MPa, $C_2 = 0.011$ and $n = 0.187$. As already mentioned, the values of these coefficients were determined from the Bridgman corrected stress-strain curve. In the tensile tests,

435   the applied force and diameters aligned with the material directions at the central cross section of the specimen were measured continuously until fracture, using an in-house measuring rig with two perpendicular lasers (for more details, see Fourmeau et al. 2011).

Figure A1 presents the comparison between the predictions and measurements of the force vs.
diameter curves in the ND direction (denoted D_z) for the smooth and notched specimens,
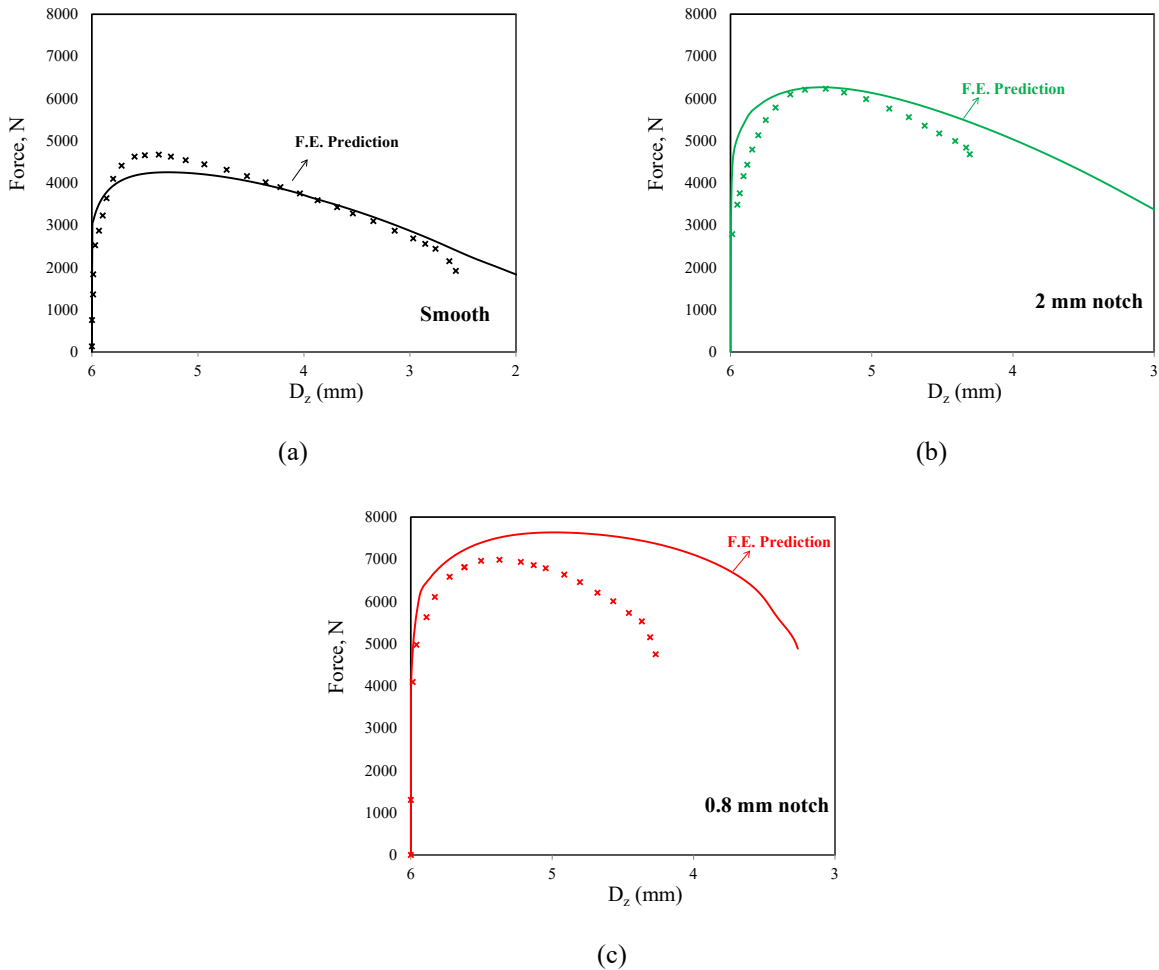respectively.

(a)

(b)

(c)

Figure A1. Comparison between data and the FE predictions of force vs. diameter curves in the
ND direction obtained using the Cazacu (2018) model in conjunction with isotropic hardening
law (Eq. (11)) with parameters determined from the Bridgman corrected stress-strain data ($C_1 =$
243.6 MPa, $C_2 = 0.011$ and $n = 0.187$): (a) smooth specimen; (b) notched specimen (2mm
notch); (c) notched specimen (0.8 mm notch). Data from Khadyko et al. (2015).

If the identification of the hardening parameters is done using the true stress-strain curve, $C_1 =$
283.6 MPa, $C_2 = 0.013$, $n = 0.22$. Additional FE simulations were performed using these values

450   of the hardening parameters, and the same values for the anisotropy coefficients involved in Cazacu (2018) orthotropic criterion (see Table 1).

Comparison between the FE predictions and experimental force vs. D_z curves for the smooth and notched specimens are given in Fig. A.2. The predictions of the diameters of the minimum cross-section along TD and ND directions for the same level of deformation as in the

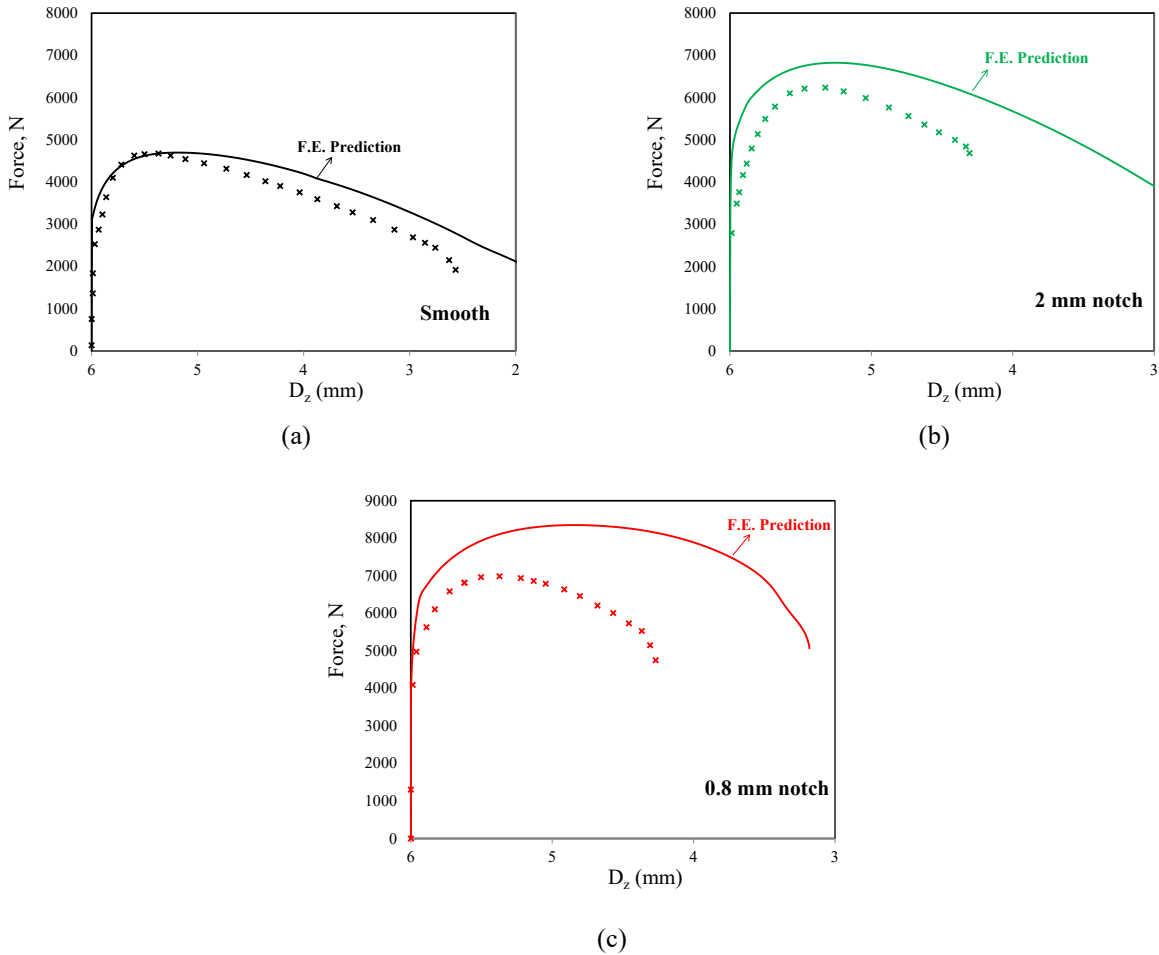455   experiments are given in Table A1.

(a)
(b)

(c)

Figure A2: Comparison between experimental and FE predictions of force vs. diameter curves obtained using the Cazacu (2018) model in conjunction with isotropic hardening law (Eq. (11)) with parameters determined from the true stress-strain data ($C_1 = 283.9$ MPa, $C_2 = 0.013$, $n = 0.22$): (a) smooth specimen; (b) notched specimen (2 mm notch); (c) notched specimen (0.8 mm

460   notch). Data from Khadyko et al. (2015).

25

Table A1: Predicted versus experimental diameters of the cross-section along TD and ND for the smooth and notched specimens obtained with Cazacu et al. (2018) criterion with anisotropy coefficients given in Table 1, and isotropic Swift hardening law (Eq. 11) with $C_1 = 283.9$ MPa, $C_2 = 0.013$, $n = 0.22$.

Specimen Type	Smooth	2 mm notch	0.8 mm notch
	Diameter along TD (mm)		
Experimental	2.97	4.07	4.11
Simulation	3.01	4.03	4.07
	Diameter along ND (mm)		
Experimental	2.04	3.51	3.63
Simulation	2.15	3.29	3.60

465

The predicted ratios between the diameters along the TD and ND directions are 1.40 for the smooth specimen, 1.22 for the 2 mm notched specimen and 1.13 for the 0.8 mm notched specimen, and respectively.

470   While the values of the hardening parameters affect the predictions of the force vs. diameter curves (compare results presented in Fig. A.1 and Fig. A.2), their influence on the predictions of the shapes of the cross-sections is negligible. Moreover, the predicted ratios of the diameters along the TD and ND directions are very close (compare Table 2 and Table A1). This is because the geometry of the deformed cross-sections is dictated by the material anisotropy.

Appendix 3: Mesh refinement study

475   A mesh-sensitivity study was also performed. It was found that further refinement of the mesh did not change the results. As an example, below are shown the cross-section prediction for 0.8 mm notch specimen modeled with (a) 9984 & (b) 14112 C3D8R elements. Note that further refinement of the mesh has negligible influence on the results (see Fig. A3).

(a)
(b)
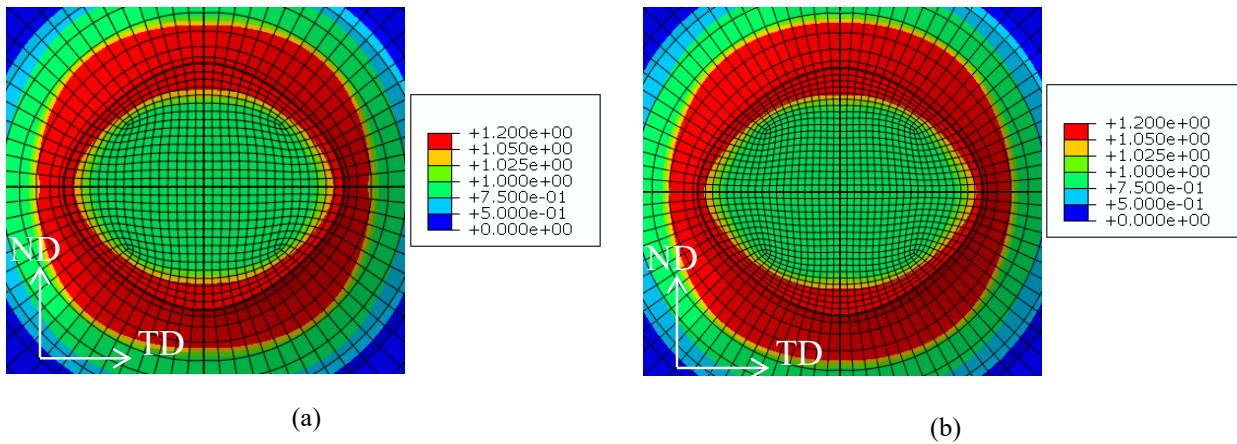
Figure A3: Cross-section prediction for 0.8 mm notch specimen modeled with (a) 9984 C3D8R elements and (b) 14112 C3D8R elements.

References

Abaqus, 2009. User's Manual for Version 6.8 vols. I-V. Dassault Systemes Simulia Corp., Providence, RI.

Barlat, F., Aretz, H., Yoon, J. W., Karabin, M. E., Brem, J. C., Dick, R. E. (2005) Linear transfomation-based anisotropic yield functions. International Journal of Plasticity 21:1009–1039.

Cazacu O (2018) New yield criteria for isotropic and textured metallic materials. International Journal of Solids and Structures 139:200–210.

Cazacu O, Barlat F (2001) Generalization of Drucker's Yield Criterion to Orthotropy. Mathematics and Mechanics of Solids 6:613–630.

Cazacu O, Revil-Baudard B, Chandola N (2018) A yield criterion for cubic single crystals. International Journal of Solids and Structures 151:9–19.

Cazacu O, Revil-Baudard B, Chandola N (2019) Plasticity-Damage Couplings: From Single Crystal to Polycrystalline Materials.

27

Chandola N, Cazacu O, Revil-Baudard B (2017) New polycrystalline modeling as applied to textured steel sheets. Mechanics Research Communications 84:98–101.

Chandola N, Cazacu O, Revil-Baudard B (2018) Prediction of plastic anisotropy of textured polycrystalline sheets using a new single-crystal model. Comptes Rendus Mécanique 346:756–769.

Engler O, Randle V (2009). Introduction to Texture Analysis: Macrotexture, Microtexture, and Orientation Mapping, second ed. CRC press, Taylor & Francis Group.

Fourmeau M, Børvik T, Benallal A, Hopperstad OS (2013) Anisotropic failure modes of high-strength aluminium alloy under various stress states. International Journal of Plasticity 48:34–53.

Fourmeau M, Børvik T, Benallal A, Lademo OG, Hopperstad OS (2011) On the plastic anisotropy of an aluminium alloy and its influence on constrained multiaxial flow. International Journal of Plasticity 27:2005–2025.

Frodal BH, Pedersen KO, Børvik T, Hopperstad OS (2017) Influence of pre compression on the ductility of AA6xxx aluminium alloys. Int. J. Fract. 206: 131–149.

Green AE, Naghdi PM (1965) A general theory of an elastic-plastic continuum. Archive for Rational Mechanics and Analysis 18:251–281.

Hannard F, Pardoen T, Maire E, Le Bourlot C., Mokso R, Simar A (2016) Characterization and micromechanical modelling of microstructural heterogeneity effects on ductile fracture of 6xxx aluminium alloys, Acta Materialia 103:558 – 572.

Hosford WF (1972) A generalized isotropic yield criterion. J Appl Mech 39:607–609

Hughes, T.J., (1984) Numerical implementation of constitutive models: rate-independent deviatoric plasticity. In Theoretical foundation for large-scale computations for nonlinear material behavior, 29-63. Springer, Dordrecht.

I-Shih, L., (1982) On representations of anisotropic invariants. International Journal of Engineering Science 20, 1099–1109.

Khadyko M, Dumoulin S, Børvik T, Hopperstad OS (2015) Simulation of large-strain behaviour of aluminium alloy under tensile loading using anisotropic plasticity models. Computers & Structures 157:60–75.

Khadyko M, Dumoulin S, Cailletaud G, Hopperstad OS (2016) Latent hardening and plastic anisotropy evolution in AA6060 aluminium alloy. International Journal of Plasticity 76:51–74.

Kohar CP, Brahme A, Hekmat F, Mishra RK, Inal K (2019) A computational mechanics engineering framework for predicting the axial crush response of Aluminum extrusions. Thin-Walled Structures 140:516–532.

Morin D, Fourmeau M, Børvik T, Benallal A, Hopperstad OS (2018) Anisotropic tensile failure of metals by the strain localization theory: An application to a high-strength aluminium alloy. European Journal of Mechanics / A Solids 69:99–112.

Smith GF, Rivlin RS (1958) The Strain-Energy Function for Anisotropic Elastic Materials. Transactions of the American Mathematical Society 88:175–193.

Wang C-C (1970) A new representation theorem for isotropic functions: An an-swer to Professor GF Smith's criticism of my papers on representations for isotropic functions. Arch Ration Mech Anal 36:166–197

Zhang H, Diehl M, Roters F, Raabe D (2016) A virtual laboratory using high resolution crystal plasticity simulations to determine the initial yield surface for sheet metal forming operations. International Journal of Plasticity 80: 111–138.

Zhang K, Holmedal B, Hopperstad OS, Dumoulin S, Gawad J, Van Bael A, Van Houtte P (2015) Multi-level modelling of mechanical anisotropy of commercial pure aluminium plate: crystal plasticity models, advanced yield functions and parameter identification. International Journal of Plasticity 66:3–30.